*Korean J. Chem. Eng.*, 39(5), 1248-1256 (2022)
DOI: 10.1007/s11814-021-1042-7

pISSN: 0256-1115
eISSN: 1975-7220

# PVP-assisted hydrothermal synthesis of $BiOCl/Bi_2Mo_3O_{12}$ photocatalyst for decolorization of rhodamine B under visible-light irradiation

**Azadeh Khane*, Nemat Tahmasebi**,†, and Hesam Seyed Kaboli*,†**

*Department of Civil Engineering, Jundi-Shapur University of Technology, Dezful, Iran
**Department of Physics, Jundi-Shapur University of Technology, Dezful, Iran
(*Received 2 August 2021 • Revised 6 December 2021 • Accepted 13 December 2021*)

**Abstract**−This study pioneered the synthesis of $BiOCl/Bi_2Mo_3O_{12}$ as a composite photocatalyst using a simple one-step hydrothermal method with polyvinylpyrrolidone (PVP) as a structure-directing agent. Characterizing the synthesized samples using different physical and chemical techniques indicated the presence of PVP in reaction solution is beneficial to growth $Bi_2Mo_3O_{12}$ phase. In addition, the synthesized samples in the presence of PVP display a red-shift in the bandgap, which improves light absorption in the visible region. The photocatalytic performance of the samples was investigated in terms of the decolorization of rhodamine B (RhB) under visible light irradiation. Comparing the photocatalytic performance of synthesized samples using different PVP amounts (0-0.5 g) showed their optimal performance in the presence of 0.1 g of PVP. Results indicated that nearly 98% of RhB was degraded within 60 min under visible light irradiation. The pH effect of the RhB solution and catalyst amount on photocatalytic performance were also investigated, and active species trapping determined the main species participating in photocatalytic reactions.

Keywords: Hydrothermal, $BiOCl/Bi_2Mo_3O_{12}$, Polyvinylpyrrolidone, Visible Light, Photocatalytic Activity

## INTRODUCTION

Environmental pollution caused by recent industrial development has caused numerous problems in human communities [1,2]. Water contamination constitutes the main challenge and a major threat to human life. Given the need for unconventional waters such as saltwater, brackish water and industrial and agricultural wastewater as a result of the water shortage crisis in recent decades, developing cost-effective, safe and efficient methods for degrading or eliminating contaminants is crucial [3,4]. In the last decades, reverse osmosis, adsorption, chemical and biological precipitation and membrane filtration have been used to eliminate contaminants from industrial wastewaters [5-7]. On the other hand, biological processes do not effectively remove the contaminants, and conventional processes such as coagulation/flocculation and adsorption cause secondary water contamination by leaving solid waste residues [8,9]. Today, the photocatalytic properties of semiconductors as an environmentally-friendly technology are utilized to efficiently degrade water contaminants [10-13].

Recent research suggests high photocatalytic performance and stability, cost-effectiveness and environmental compatibility make bismuth-based semiconductors, such as $Bi_2WO_6$, $Bi_2O_3$, BiOCl, BiOBr and BiOI, effective candidates for photocatalytic applications [14-19]. Moreover, the layered structure and unique electrical, optical and photocatalytic properties of BiOCl have attracted the attention of researchers. BiOCl structurally comprises alternate layers of $[Bi_2O_2]$-$[Cl_2]$, which develops a strong electric field between $[Bi_2O_2]^{2-}$ and $Cl^{-1}$ layers. This electric field effectively separates electrons from holes in generated electron-hole pairs and improves the photocatalytic performance of the compound [20-22]. As a photocatalytic disadvantage of BiOCl, its relatively-broad band gap (3.3 eV) causes excitation and formation of electron-hole pairs to occur only under ultraviolet irradiation [23,24]. Note that the ultraviolet (UV) spectrum accounts for nearly 6% of solar energy in the spectrum, and visible wavelengths account for about 50% of solar energy [25,26]. Using visible light-active photocatalysts is therefore crucial for the optimal application of solar energy [27,28]. The methods so far reported for activating BiOCl under visible light irradiation include morphological modification, metal and non-metal ion doping, creating oxygen vacancies and combining this semiconductor with other semiconductors [29-33]. Among them, the coupling of two or more semiconductors to create a heterostructure is considered effective for improving their photocatalytic performance [34-39]. BiOCl has been frequently used as a photocatalyst in coupling with other semiconductors such as $Bi_2WO_6$, $CeO_2$, $TiO_2$, $SnO_2$ and ZnO [40-44]. Tahmasebi et al. used a simple hydrothermal method to synthesize $Bi_2WO_6$/BiOCl composite photocatalyst. They reported no photocatalytic response to visible light in pure BiOCl and found $Bi_2WO_6$/BiOCl to effectively degrade RhB molecules under visible light irradiation [40]. Zhang et al. found $BiOCl/CeO_2$ as a composite photocatalyst synthesized with co-precipitation to effectively degrade RhB molecules under simulated solar irradiation [41]. Sanchez et al. found BiOCl-$TiO_2$ synthesized as a composite photocatalyst using the sol-gel method to outperform pure BiOCl and $TiO_2$ in degrading phenol molecules under visible light irradiation [42].

The crystalline phases of bismuth molybdate as a semiconductor include $\alpha$-$Bi_2Mo_3O_{12}$, $\beta$-$Bi_2Mo_2O_6$ and $\gamma$-$Bi_2MoO_6$ [44,45]. Rapid movement of carriers in the layered structure of $\alpha$-$Bi_2Mo_3O_{12}$ with

†To whom correspondence should be addressed.
E-mail: tahmasebi@jsu.ac.ir, hkaboli@jsu.ac.ir

a bandgap of 2.5-2.9 eV has increased the application of this n-type semiconductor in photocatalytic processes [46,47]. To the best of the authors' knowledge, $BiOCl/Bi_2Mo_3O_{12}$ has not been yet synthesized as a composite semiconductor.

The present study was therefore conducted to synthesize $BiOCl/Bi_2Mo_3O_{12}$ using a simple one-step hydrothermal method and investigate the photocatalytic performance of this compound in degrading RhB molecules in water under visible light irradiation. The crystalline structure, morphology and chemical composition of the samples were characterized using X-ray powder diffraction (XRD), scanning electron microscopy (SEM) and energy dispersive X-ray spectroscopy (EDS), and their optical and light absorption properties using diffuse reflectance spectroscopy (DRS) and photoluminescent (PL). Active species trapping was also used to identify active species generated in photocatalyst process under visible light for degradation of dye molecules.

## EXPERIMENTS

### 1. Materials

Sodium molybdate ($Na_2MoO_4$), bismuth nitrate pentahydrate ($Bi(NO_3)_3{\cdot}5H_2O$), hydrochloric acid (HCl), PVP (MW=1,300,000) and RhB were purchased from Sigma-Aldrich Company. The high purity of the materials used to obviate the need for their further purification. Deionized water with a resistance of 18 MΩ-cm was used in all stages of the experiments. HCL and NaOH were used to adjust the pH of the RhB solution.

### 2. Sample Preparation

Solution A, prepared by dissolving 1.2 g of $Na_2MoO_4$ in 50 ml of deionized water, was stirred on a magnetic stirrer for 70 min. Solution B, prepared by dissolving 0, 0.1, 0.3 and 0.5 g of PVP in 50 ml of deionized water, was stirred on a magnetic stirrer for 15 min. After 1.6 ml of HCl and 2.82 g of $Bi(NO_3)_3{\cdot}5H_2O$ was added to solution B, it was stirred on a magnetic mixer for 15 min at 60 °C, added to solution A drop by drop and mixed on a magnetic stirrer for 10 min. A 100-ml Teflon-lined stainless autoclave containing 80 ml of the final solution was placed in a 180 °C oven for 12 h. The autoclave was then cooled at room temperature. The product was collected with a centrifuge, rinsed with deionized water several times and eventually dried at 80 °C. The products synthesized with 0, 0.1, 0.3 and 0.5 g of PVP were, respectively, labeled as P-0, P-0.1, P-0.3 and P-0.5. For comparison, the pure-BiOCl sample was synthesized using the same procedure without adding sodium molybdate.

### 3. Characterization

The crystal structure of the synthesized powders was evaluated using X-ray diffraction (XRD, A Phillips diffractometer-PW1730) equipped with a Cu K$\alpha$ radiation ($\lambda$=1.54178 Å) and operated at 40 mV and 30 mA. The Fourier-transform infrared spectroscopy (FTIR) spectra were recorded by Thermo Nicolet Avatar infrared spectrometer. The morphology of the samples was observed using FESEM (TESCAN Mira3). Moreover, the chemical composition of the samples was investigated using energy dispersive spectroscopy (EDS, TESCAN MIRA II). The UV-vis light absorption properties of the samples were recorded by UV-vis DRS (Avaspec-2048-TEC model). The PL spectra of the samples were recorded by a JASCO FP-6500 spectrometer at the excitation wavelength of 270 nm.

### 4. Photocatalytic Test

The photocatalytic activity of the samples was examined through the photocatalytic degradation of RhB under visible light irradiation. The source of visible light was a 55-W xenon lamp equipped with a 400-nm filter for eliminating UV radiation. Every experiment was performed by adding 40 mg of the powder samples to 40 ml of the RhB solution with an initial concentration of 10 mg/L. A magnetic stirrer was used to uniformly distribute the photocatalytic particles in the solution. The solution was placed in an ice-water bath to counteract the effect of thermal degradation of RhB molecules under light irradiation. The distance between the lamp and the solution was 15 cm. Before the light irradiation, the solution containing the photocatalyst was kept in the dark for 1 h to ensure the adsorption/desorption equilibrium between the dye molecules and photocatalyst surface. Two mL of the solution was then sampled at specific time points after irradiation to analyze the concentration of the dye molecules. The photocatalytic performance was calculated using the following equation:

$$\eta\,(\%)=[(C_0-C)/C_0]\times 100 \quad (1)$$

where $C_0$ and C, respectively, represent the RhB concentration at baseline and after light irradiation.

## RESULTS AND DISCUSSION

### 1. Characterization of Samples

The phase and crystalline structure of the samples were analyzed using XRD. Fig. 1 shows the XRD patterns of the samples synthesized with different PVP amounts. Most of the peaks in the XRD pattern of P-0 corresponded to the tetragonal crystalline phase of BiOCl (JCPDS Card No. 06-0249). In addition, three weak peaks observed at $2\theta$=28.4°, 29.6° and 31.4°, and marked with arrows were associated with $Bi_2Mo_3O_{12}$ with a monoclinic crystalline struc-

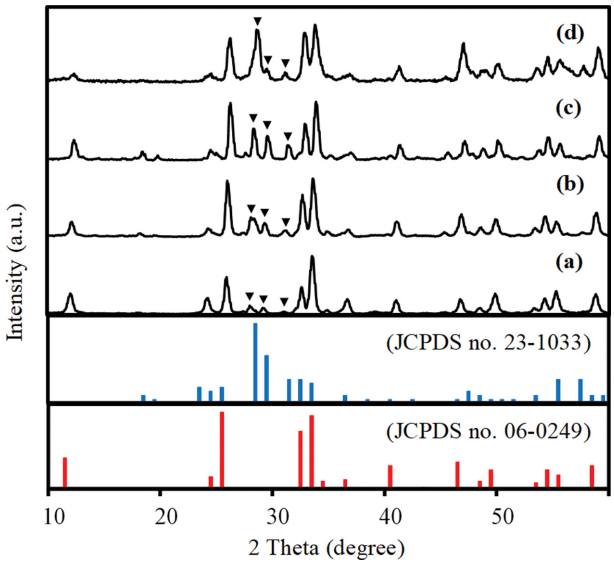


**Fig. 1. XRD patterns of samples (a) P-0, (b) P-0.1, (c) P-0.3, (d) P-0.5.**

**Table 1. EDS analysis of synthesized samples**

| | Atomic percent (%) | | | | Mo/Bi ratio |
|---|---|---|---|---|---|
| | O Ka | Cl Ka | Mo La | Bi Ma | |
| P-0 | 48.30 | 23.10 | 6.74 | 21.86 | 0.31 |
| P-0.1 | 50.34 | 20.16 | 7.95 | 21.55 | 0.37 |
| P-0.3 | 52.88 | 17.86 | 8.48 | 20.78 | 0.41 |
| P-0.5 | 60.39 | 12.38 | 9.00 | 18.23 | 0.49 |

ture (JCPDS Card No. 23-1033). For comparison, the XRD pattern of pure-BiOCl is displayed in Fig. S1. XRD patterns of P-0.1, P-0.3 and P-0.5 in Fig. 1(b)-(d) show negligible change in the peaks of the crystalline structure of BiOCl in the presence of PVP; in contrast, increasing the amount of PVP increased the diffraction peaks of the monoclinic crystalline structure of $Bi_2Mo_3O_{12}$, which indicated the beneficial of PVP for formation of $Bi_2Mo_3O_{12}$ phase. It is well known that PVP can act as a structure-directing agent [48-50]. Thus, it can be concluded that the presence of PVP molecules in the reaction solution and their adsorption on nanoparticles during clustering developed the content of $Bi_2Mo_3O_{12}$ phase in $BiOCl/Bi_2Mo_3O_{12}$ composite.

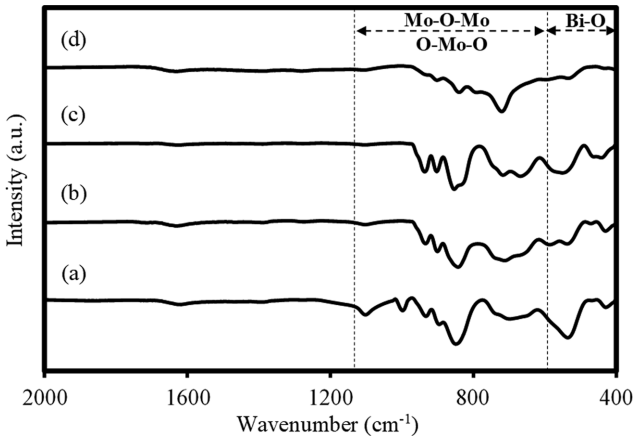


**Fig. 2. The FTIR spectra of samples (a) P-0, (b) P-0.1, (c) P-0.3, (d) P-0.5.**

Table 1 and Fig. S2 show the chemical composition of the synthesized samples determined using EDS analysis. Chemical purity

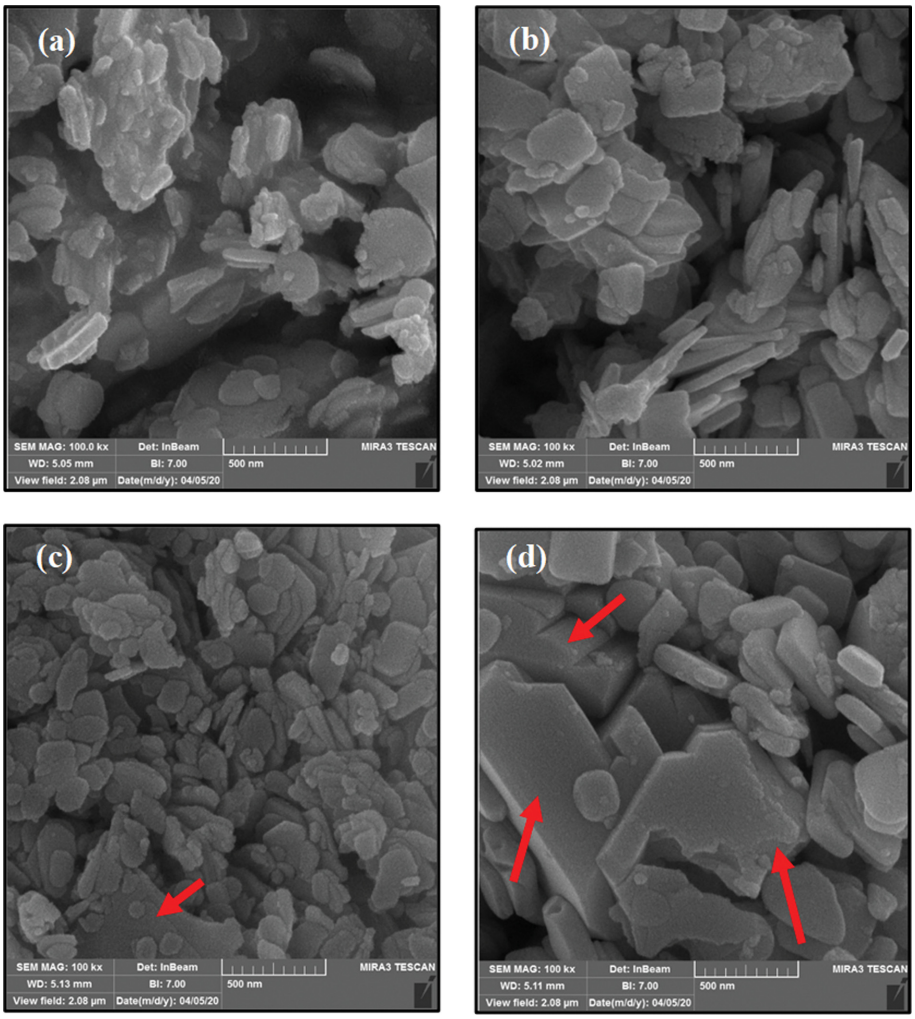


**Fig. 3. The SEM images of samples (a) P-0, (b) P-0.1, (c) P-0.3, (d) P-0.5.**

of the samples was confirmed by observing only O, Cl, Bi and Mo in their composition. According to the last column of Table 1, the MO/Bi atomic ratio was 0.31 in P-0, 0.37 in P-0.1, 0.41 in P-0.3 and 0.49 in P-0.5, indicating the increase of Mo-to-Bi molar ratio with increasing the amount of PVP in reaction solution. These results, in line with the XRD data, confirm the growth of the $Bi_2Mo_3O_{12}$ phase in $BiOCl/Bi_2Mo_3O_{12}$ with the increasing of PVP. Furthermore, as shown in Fig. S2(f), the elemental mapping analysis clearly reveals the highly uniform distribution of Bi, Mo and Cl elements, which confirms that the BiOCl and $Bi_2Mo_3O_{12}$ are successfully composited and a $BiOCl/Bi_2Mo_3O_{12}$ mixed-phase has been formed.

Fig. 2 shows the results of FTIR performed to identify chemical bonds in the samples. The main peaks of P-0 were observed at 534, 717, 846, 898, 933 and 997 $cm^{-1}$. The peak at 534 $cm^{-1}$ is related to the Bi-O bond in BiOCl [51] and the peaks found at 717, 846, 898, 933 and 997 $cm^{-1}$ are associated with Mo-O-Mo or O-Mo-O bonds in the $Bi_2Mo_3O_{12}$ compound [52-54]. According to Fig. 3, increasing the amount of PVP, respectively, decreased and increased the peak intensity of the Bi-O bond and the oxygen-molybdenum bonds in $BiOCl/Bi_2Mo_3O_{12}$. Observing the main peak of P-0.5 at higher levels (720 $cm^{-1}$) than that of P-0.1 and P-0.3 could be attributed to the changes in the octahedral structure and oxygen-molybdenum bonds of $MoO_6$ at higher amounts of PVP.

The morphology of samples was examined using FESEM analysis. Fig. 3 displays the FESEM images of the samples synthesized with different amounts of PVP. It can be seen the P-0 sample is composed of aggregated nanoparticles in the absence of PVP. Thus, PVP is used as an indispensable capping agent to prevent particle aggregation [55,56]. Fig. 3(b)-(c) indicates that the synthesized samples in the presence of PVP display more uniform morphology due to the growth modifier effect of PVP [55,56]. It is observed the P-0.1 sample comprises 50-nm thick nanoplates, whereas the P-0.3 and P-0.5 are composed of micro-cubes (marked with arrows) along with nanoplates, which the number of micro-cubes has increased for P-0.5 sample. It can be said increasing the amount of PVP in P-0.3 and P-0.5 developed nanoplates in different directions and formed $Bi_2Mo_3O_{12}$ micro-cubes due to the growth modifier effect of PVP.

The nitrogen adsorption-desorption method was applied to investigate the porous structure of the samples. As shown in Fig. S3, all the adsorption-desorption isotherms display type-IV curves with H3 hysteresis loop, which displays the existence of mesopores [57]. The surface area of P-0, P-0.1 and P-0.5 is 4.492 $cm^3g^{-1}$, 6.540 $cm^3g^{-1}$ and 8.472 $cm^3g^{-1}$, respectively, which indicates the specific surface area of the samples are nearly the same (Table 2).

The amount of incident light absorbed on the surface of a semiconductor affects its photocatalytic performance and the number

**Table 2. BET surface area, pore volume and pore diameter of P-0, P-0.1 and P-0.5 samples**

| Sample | $S_{BET}$ ($m^2g^{-1}$) | Pore volume ($cm^3g^{-1}$) | Pore diameter (nm) |
|---|---|---|---|
| P-0 | 4.492 | 0.031 | 27.702 |
| P-0.1 | 6.540 | 0.047 | 28.826 |
| P-0.5 | 8.472 | 0.068 | 34.66 |

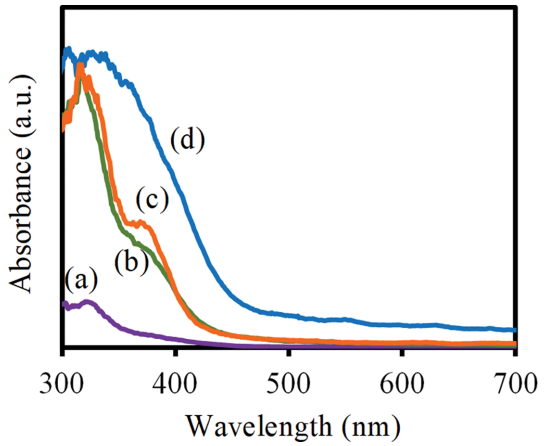


**Fig. 4. UV-vis diffuses reflectance spectra of samples, (a) P-0, (b) P-0.1, (c) P-0.3, (d) P-0.5.**

of electron-hole pairs generated. The present study employed UV-vis DRS to investigate the optical properties of the semiconductor powders. Fig. 4 shows the absorption spectra of the synthesized samples, suggesting the higher absorption intensity of the synthesized samples in the presence of PVP compared to that of P-0 at a wavelength of 300-500 nm. A red-shift was also observed in the absorption edge of the synthesized samples in the presence of PVP. It can be said these samples have a better ability to absorb visible light, so it is predicted to display better photocatalytic activities for the degradation of organic molecules such as RhB.

Tauc plot method was used to determine the bandgap of the samples [58,59]. According to this method, the band gap energy ($E_g$) of powder samples can be estimated by $(\alpha h\nu)^{1/n}=A(h\nu-E_g)$, where $\alpha$ is the absorption coefficient, hv is the energy of the incident photon, n depends on the electron transition in a semiconductor (n=0.5 for direct transition and n=2 for indirect transition), and A is a constant. The bandgap energy of the semiconductors was estimated based on the intersection of tangent lines to the linear parts of each curve with the energy axis.

The band gap energy of pure BiOCl with the energy gap of 3.25 eV in UV region is displayed in Fig. S4. According to the tangent lines to the curve of P-0 in Fig. 5(a), in addition to a band gap at 3.1 eV in the UV region, a shoulder associated with a band gap in the visible spectrum appeared. The observation of two prominent band gaps for composite material previously has been reported [60,61]. Thus, the observed band gap at UV and Vis regions could be attributed to the BiOCl and $Bi_2Mo_3O_{12}$ component in $BiOCl/Bi_2Mo_3O_{12}$ composite, respectively. Moreover, the shoulders of the visible spectrum in P-0.1 and P-0.3, respectively, shown in Fig. 5(b) and (c), are associated with increasing amounts of $Bi_2Mo_3O_{12}$ in $BiOCl/Bi_2Mo_3O_{12}$. According to Fig. 5(d), the shoulders of the UV and visible band gaps are not distinguishable in P-0.5, and the tangent line to the curve shows only one band gap in the visible region. This phenomenon can be explained by increased optical absorption at 300-500 nm in the presence of $Bi_2Mo_3O_{12}$ compared to in BiOCl, which confirms the phase increase of $Bi_2Mo_3O_{12}$ in P-0.5 sample.

Photoluminescence (PL) emission spectra were employed to

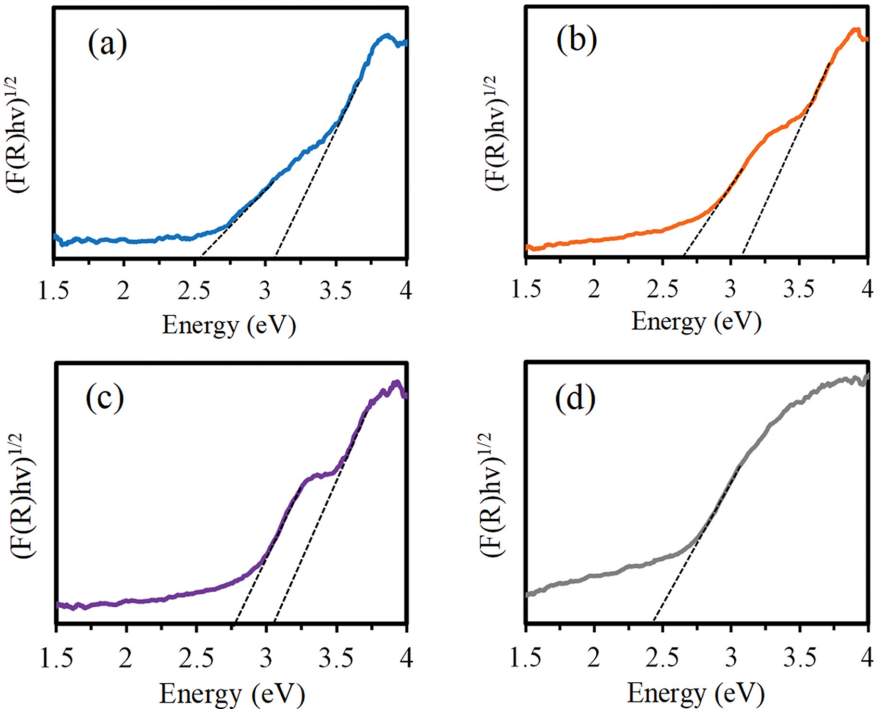


**Fig. 5. The band gap energy of samples (a) P-0, (b) P-0.1 g, (c) P-0.3 g, (d) P-0.5.**

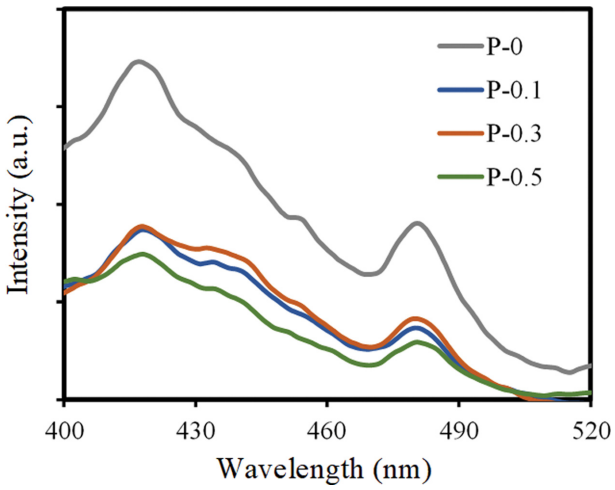


**Fig. 6. PL emission spectra of samples at an excitation wavelength of 270 nm.**

investigate the recombination of photogenerated electron-hole pairs. The higher PL intensity indicates the higher recombination rate of electrons and holes. Fig. 6 displays the PL emission spectra of the samples, suggesting the recombination rate of electrons and holes in P-0 sample is higher than other samples.

**2. Photocatalytic Performance**

In this study, the photocatalytic ability of the samples was investigated for decomposition of RhB as a model pollutant under visible light irradiation. The intensity of the absorption peak at 554 nm was used as a measure of the concentration of RhB molecules in water [62,63]. Fig. 7 displays the temporal evolution of the absorption spectra of RhB solution in the presence of P-0.1. The decrease observed in the intensity of the RhB absorption peak under light radiation in Fig. 7(a) reflects a decrease in the concentration of RhB molecules as a result of their photocatalytic degradation. Elimination and photocatalytic degradation rates can be used to compare the photocatalytic performance of different semiconductors, including the synthesized photocatalysts (Fig. 7(b) and (c)). No changes were, however, observed in the concentration of the RhB solution under light irradiation in the absence of the photocatalyst, indicating very low degradation of RhB under visible light irradiation (i.e., no photolysis). The photocatalytic performance in dye degradation was obtained as 20% in P-0, 99% in P-0.1, 86% in P-0.3 and 85% in P-0.5. The photocatalytic performance of the sample synthesized with 0.1 g of PVP (P-0.1) in degrading RhB molecules was therefore the highest and that of the sample containing no PVP (P-0) the lowest. Using PVP in synthesizing the samples was therefore found to significantly improve their photocatalytic activity. As mentioned, the photocatalytic degradation rate can be used to compare the performance of photocatalysts. This index was calculated as the slope of the $Ln(C/C_0)$ curve versus irradiation time.

$$-Ln(C/C_0)=kt \quad (2)$$

where k represents the degradation rate and $C_0$ and C. respectively. denote the concentration of the RhB solution before and after the photocatalytic reaction. Fig. 7(c) shows $Ln(C/C_0)$ versus irradiation time and Fig. 7(d) represents the degradation rate (k) of different photocatalysts. According to Fig. 7(d), k equals 0.002 for P-0, 0.054 for P-0.1, 0.016 for P-0.3 and 0.010 for P-0.5. The photocatalytic degradation rate of P-0.1 therefore equals 27 times that of P-0, 3.3 times that of P-0.3 and 5.4 times that of P-0.5. Thus, it is expected the incorporating PVP into the characterized sam-

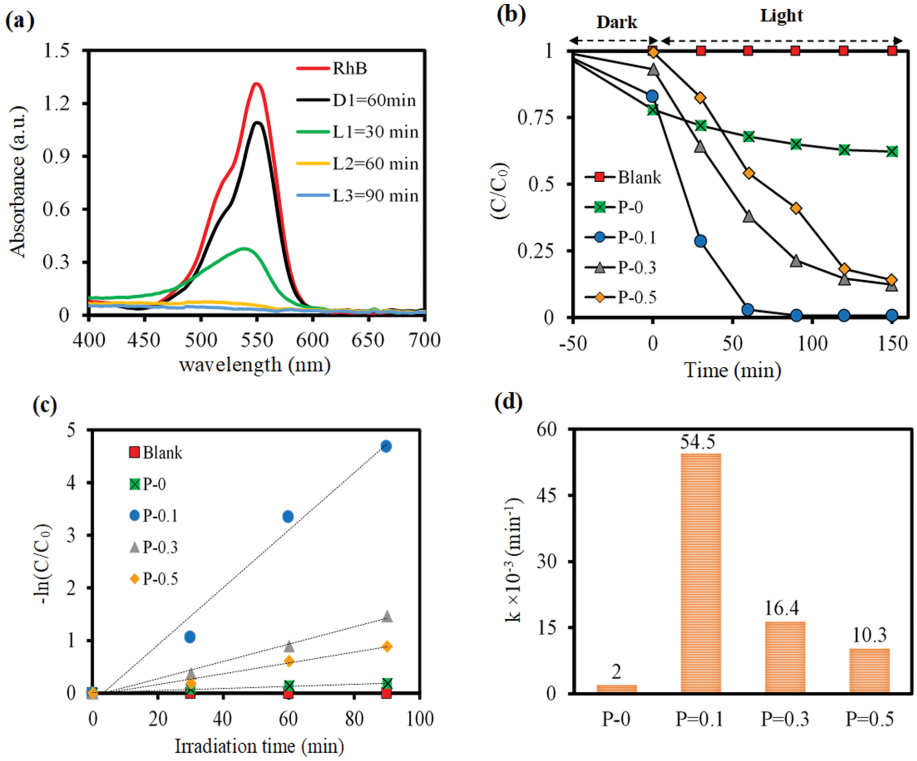


**Fig. 7. (a) The UV-vis absorption spectra of RhB solution under light irradiation in the presence of P-0.1 sample, (b) photocatalytic degradation of RhB under visible light in the presence of synthesized samples, the corresponding (c) $-Ln(C/C_0)$ versus irradiation time, and (d) the kinetic constant.**

ples increases their photocatalytic performance by optimizing the amount of $Bi_2Mo_3O_{12}$ in $BiOCl/Bi_2Mo_3O_{12}$ and improves the optical absorption to generate more electron-hole pairs under visible light.

As discussed above, the P-0.1 sample displays the highest photocatalytic performance. In the following, the main active species participating in photocatalytic reactions, the photocatalytic stability and the effect of initial RhB solution pH on photocatalytic performance of this sample are investigated.

Active species trapping was used to identify the active species involved in degrading RhB molecules. This study employed $K_2Cr_2O_7$, EDTA-2Na, tert-Butyl alcohol (TBA) and benzoquinone (BQ) to trap electrons, holes, hydroxyl radicals ($^{\bullet}OH$) and superoxide radicals ($^{\bullet}O_2$), respectively [64,65]. Trapping was performed in the same way as the photocatalytic test was conducted for RhB degradation, and its results are presented in Fig. 8(a), suggesting significant reduction in the photocatalytic performance of the composite nanoparticles of $BiOCl/Bi_2Mo_3O_{12}$ in the presence of $K_2Cr_2O_7$ and BQ. Negligible and no decreases were, however, observed in the presence of EDTA-2Na and TBA, respectively. Holes were therefore found to play an insignificant role in degrading RhB molecules, whereas electrons and superoxide radicals ($^{\bullet}O_2$) significantly contributed to this process. The mechanism of photocatalytic reactions is displayed in Fig. 8(b).

The stability of the composite photocatalyst $BiOCl/Bi_2Mo_3O_{12}$ was investigated by examining its performance in degrading RhB molecules in five consecutive cycles. According to Fig. 8(c), approximately 98% of RhB molecules were degraded within five consecutive cycles, which confirmed the stability of the sample for practical applications. In addition, as shown in Fig. 8(d), the XRD data indicated that the diffraction patterns of P-0.1 sample before and after photocatalytic reactions display negligible changes, which confirms the stability of crystalline structure after a photocatalytic reaction.

Given the significant effect of the medium pH on the photocatalytic performance of semiconductors, this section examined the performance of the synthesized composite photocatalyst $BiOCl/Bi_2Mo_3O_{12}$ in media with different pH values. HCl and NaOH were therefore used to prepare 10-ppm RhB solutions with pH=3, 7 and 11. After 40 mg of the photocatalyst was added to the RhB solutions, they were kept in the dark for 1 h and then exposed to visible light. Fig. 9(a) shows the performance of the composite photocatalyst versus pH, suggesting its higher performance in acidic than alkaline media given its negligible performance at pH=11. As is known, adsorbing RhB molecules by the surface of a photocatalyst is essential for beginning a photocatalytic reaction. In this process, RhB molecules with a positive charge are adsorbed by metal oxides with a negative charge, and interactions between RhB molecules and active electron-hole species degrade RhB molecules. At pH>7, the repulsive force developed between negatively-charged RhB molecules through attracting $OH^-$ species and negatively-charged photocatalyst surface decreases the adsorption of organic molecules by the photocatalyst [66,67]. Fig. 9(a) shows that 10%, 18% and 32% of RhB molecules were, respectively, eliminated from the RhB solution with pH=3, 7 and 11 and after being kept in the dark for one hour. Thus, the lower the pH, the higher the number

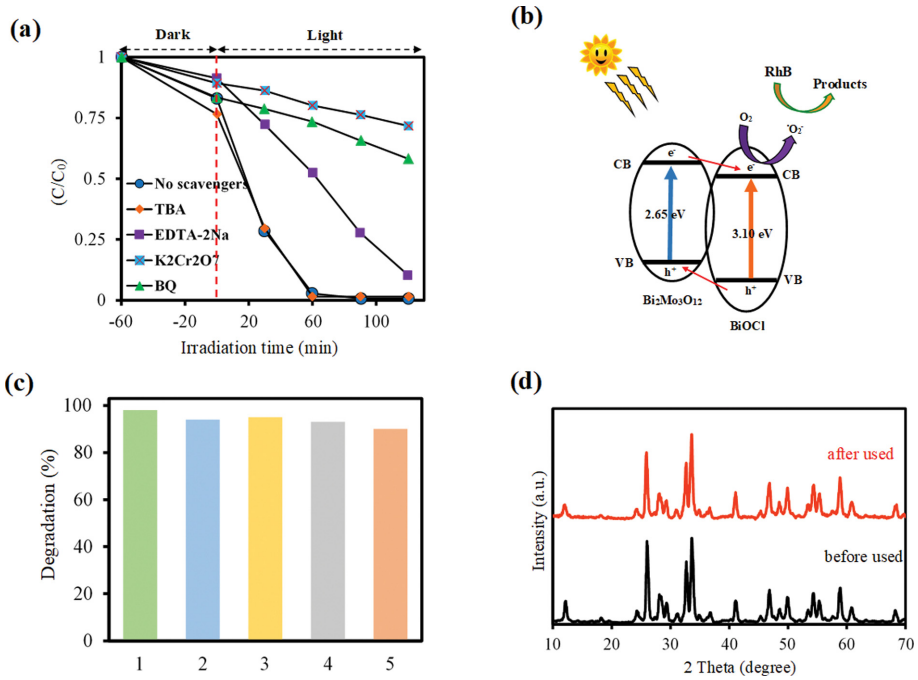


**Fig. 8. (a) The effect of different scavengers on the photocatalytic activity of P-0,1 sample, (b) schematic diagram of photocatalytic reactions over P-0.1, (c) the recycle experiments in five successive cycles, and (d) XRD pattern of P-0.1 sample before and after photocatalytic reactions.**

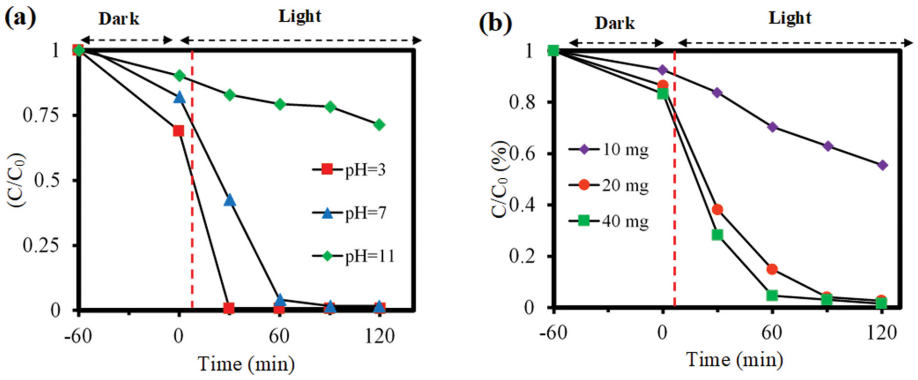


**Fig. 9. (a) The effect of pH of RhB solution and (b) catalyst amount on the degradation of RhB under visible light irradiation in the presence of P-0.1 sample.**

of RhB molecules adsorbed by the photocatalyst and the better the photocatalytic performance.

To investigate the effect of catalyst amount on the photocatalytic degradation of RhB, different amount of P-0.1 sample (from 10 to 40 mg) was added to 40 mL of RhB solution with initial concentration of 10 mg/L. As shown in Fig. 9(b) the photocatalytic degradation of RhB solution increased with increasing the amount of photocatalyst. This behavior is attributed to the increase in the number of available active sites for adsorption and degradation of RhB molecules.

## CONCLUSION

$BiOCl/Bi_2Mo_3O_{12}$ was synthesized as a composite photocatalyst using the one-step hydrothermal method. Characterizing the samples showed the significant effect of PVP on their phase composition, morphology and optical characteristics. Investigating the photocatalytic performance of the samples synthesized with different amounts of PVP showed the highest efficiency in degrading RhB molecules under visible light irradiation in a sample synthesized in the presence of 0.1 g of PVP. It is suggested that incorporating PVP into the characterized samples increased their photocatalytic performance by optimizing the amount of $Bi_2Mo_3O_{12}$ in $BiOCl/Bi_2Mo_3O_{12}$ composite, which led to improving the optical absorption to generate more electron-hole pairs and decreasing the recombination rate of electrons and holes. Examining the pH effect of the dye solution on the photocatalytic performance also showed the appropriate performance of the sample at pH<7 and its poor

performance in alkaline media. Identifying active species ultimately found electrons and superoxide radicals ($^{\bullet}O_2$) to play key roles in degrading RhB molecules.

## DECLARATION OF COMPETING INTEREST

The authors declare that they have no known competing financial interests or personal relationships that could have appeared to influence the work reported in this paper.

## SUPPORTING INFORMATION

Additional information as noted in the text. This information is available via the Internet at http://www.springer.com/chemistry/journal/11814.

## REFERENCES


1. A. Hazrat, *Water Air Soil Pollut.*, **213**, 251 (2010).
2. M. Kousha, S. Tavakoli, E. Daneshvar, A. Vazirzadeh and A. Bhatnagar, *J. Mol. Liq.*, **207**, 266 (2015).
3. S. Panimalar, R. Uthrakumar, E. T. Selvi, P. Gomathy, C. Inmozhi, K. Kaviyarasu and J. Kennedy, *Surf. Interfaces*, **20**, 100512 (2020).
4. N. Geetha, S. Sivaranjani, A. Ayeshamariam, M. Siva Bharathy, S. Nivetha, K. Kaviyarasu and M. Jayachandran, *J. Adv. Microsc. Res.*, **13**, 12 (2018).
5. M. A. Al-Ghouti, M. A. Al-Kaabi, M. Y. Ashfaq and D. A. Da'na, *J. Water Process. Eng.*, **28**, 222 (2019).
6. Y. Wen, J. Yuan, X. Ma, S. Wang and Y. Liu, *Environ. Chem. Lett.*, **17**, 1539 (2019).
7. N. Tahmasebi and M. Khalildashti, *Korean J. Chem. Eng.*, **37**, 448 (2020).
8. P. Shandilya, D. Mittal, M. Soni, P. Raizada, A. Hosseini-Bandegharaei, A. K. Saini and P. Singh, *J. Clean. Prod.*, **203**, 386 (2018).
9. J. You, Y. Guo, R. Guo and X. Liu, *Chem. Eng. J.*, **373**, 624 (2019).
10. L. Zhang, J. Ran, S. Z. Qiao and M. Jaroniec, *Chem. Soc. Rev.*, **48**, 5184 (2019).
11. Y. Cho, H. J. Lee and S. Sung, *Korean J. Chem. Eng.*, **37**, 1071 (2020).
12. W. Zhong, B. Xiao, Z. Lin, Z. Wang, L. Huang, S. Shen, Q. Zhang and L. Gu, *Adv. Mater.*, **33**, 2007894 (2021).
13. Z. Wang, Z. Lin, J. Deng, S. Shen, F. Meng, J. Zhang, Q. Zhang, W. Zhong and L. Gu, *Adv. Energy Mater.*, **11**, 2003023 (2021).
14. M. Arumugam, T. S. Natarajan, T. Saelee, S. Praserthdam, M. Ashokkumar and P. Praserthdam, *Chemosphere*, **282**, 131054 (2021).
15. H. Chawla, A. Chandra, P. P. Ingole and S. Garg, *J. Ind. Eng. Chem.*, **95**, 1 (2021).
16. X. Ren, K. Wu, Z. Qin, X. Zhao and H. Yang, *J. Alloys Compd.*, **788**, 102 (2019).
17. L. Derikvand and N. Tahmasebi, *Korean J. Chem. Eng.*, **38**, 163 (2021).
18. Y. Cui, L. Yang, Y. Yan, Z. Wang, J. Zheng, B. Li, Y. Feng, C. Li and M. Meng, *Korean J. Chem. Eng.*, **38**, 442 (2021).
19. T. Narenuch, T. Senasu, T. Chankhanittha and S. Nanan, *J. Solid State Chem.*, **294**, 121824 (2021).
20. L. Sun, L. Xiang, X. Zhao, C. J. Jia, J. Yang, Z. Jin, X. Cheng and W. Fan, *ACS Catal.*, **5**, 3540 (2015).
21. M. A. Gondal, C. Xiaofeng and M. A. Dastageer, *Novel bismuth-oxyhalide-based materials and their applications*, Springer, India (2017).
22. T. Senasu, T. Narenuch, K. Wannakam, T. Chankhanittha and S. Nanan, *J. Mater. Sci. Mater. Electron.*, **31**, 9685 (2020).
23. Y. Huang, H. Xu, D. Luo, Y. Zhao, Y. Fang, Q. Guo, Y. Wei, L. Fan and J. Wu, *J. Alloy Compd.*, **806**, 418 (2019).
24. J. Mei, Y. Tao, C. Gao, Q. Zhu, H. Zhang, J. Yu, Z. Fang, H. Xu, Y. Wang and G. Li, *Appl. Catal. B: Environ.*, **285**, 119841 (2021).
25. B. Buchholcz, H. Haspel, A. Oszko, A. Kukovecz and Z. Konya, *RSC Adv.*, **7**, 16410 (2017).
26. J. Zhang, L. Zhang, X. Shen, P. Xu and J. Liu, *CrystEngComm*, **18**, 3856 (2016).
27. W. Liang, J. Pan, X. Duan, H. Tang, J. Xu and G. Tang, *Ceram. Int.*, **46**, 3623 (2020).
28. M. S. Hamdy, H. S. Abd-Rabboh, M. Benaissa, M. G. Al-Metwaly, A. H. Galal and M. A. Ahmed, *Opt. Mater.*, **117**, 111198 (2021).
29. J. Sun, D. Li, Y. Li, Y. Cai, L. Sun, X. Yuan, G. Cao, H. Xu and D. Xia, *ChemistrySelect*, **3**, 4463 (2018).
30. D. Zhang, S. Liang, S. Yao, H. Li, J. Liu, Y. Geng and X. Pu, *Sep. Purif. Technol.*, **248**, 117040 (2020).
31. W. Liu, Y. Shang, A. Zhu, P. Tan, Y. Liu, L. Qiao, D. Chu, X. Xiong and J. Pan, *J. Mater. Chem.*, **5**, 12542 (2017).
32. Y. Cai, D. Li, J. Sun, M. Chen, Y. Li, Z. Zou, H. Zhang, H. Xu and D. Xia, *Appl. Surf. Sci.*, **439**, 697 (2018).
33. J. Lu, Y. Wang, F. Liu, L. Zhang and S. Chai, *Appl. Surf. Sci.*, **393**, 180 (2017).
34. J. Low, J. Yu, M. Jaroniec, S. Wageh and A. A. Al-Ghamdi, *Adv. Mater.*, **29**, 1601694 (2017).
35. G. Zhang, D. Chen, N. Li, Q. Xu, H. Li, J. He and J. Lu, *Appl. Catal. B: Environ.*, **250**, 313 (2019).
36. H. S. Abd-Rabboh, M. Benaissa, M. S. Hamdy, M. A. Ahmed and M. Glal, *Opt. Mater.*, **114**, 110761 (2021).
37. F. A. Fouad, M. A. Ahmed, M. S. Antonious and M. F. Abdel-Messih, *J. Mater. Sci. Mater. Electron.*, **31**, 12355 (2020).
38. T. Chankhanittha and S. Nanan, *J. Colloid Interface Sci.*, **582**, 412 (2021).
39. J. Piriyanon, T. Chankhanittha, S. Youngme, K. Hemavibool, S. Nijpanich, S. Juabrum, N. Chanlek and S. Nanan, *J. Mater. Sci. Mater. Electron.*, **32**, 19798 (2021).
40. N. Tahmasebi, Z. Maleki and P. Farahnak, *Mater. Sci. Semicond. Process.*, **89**, 32 (2019).
41. Y. Zhang, Q. Shao, H. Jiang, L. Liu, M. Wu, J. Lin, J. Zhang, S. Wu, M. Dong and Z. Guo, *Inorg. Chem. Front.*, **7**, 1345 (2020).
42. D. Sánchez-Rodríguez, M. G. M. Medrano, H. Remita and V. Escobar-Barrios, *J. Environ. Chem. Eng.*, **6**, 1601 (2018).
43. M. Sun, Q. Zhao, C. Du and Z. Liu, *RSC Adv.*, **5**, 22740 (2015).
44. J. Q. Chang, Y. Zhong, C. H. Hu, J. L. Luo and P. G. Wang, *J. Mol. Struct.*, **1183**, 209 (2019).
45. K. Schuh, W. Kleist, M. Høj, V. Trouillet, A. D. Jensen and J. D. Grunwaldt, *Chem. Commun.*, **50**, 15404 (2014).
46. L. N. Song, L. Chen, J. He, P. Chen, H. K. Zeng, C. T. Au and S. F. Yin, *Chem. Commun.*, **53**, 6480 (2017).
47. S. U. Din, M. ul Haq, R. Khatoon, X. Chen, L. Li, M. Zhang and L. Zhu, *RSC Adv.*, **10**, 21940 (2020).
48. Y. Pang, G. Xu, Q. Feng, J. Liu, J. Lv, Y. Zhang and Y. Wu, *Langmuir*, **33**, 8933 (2017).

49. W. Liu, S. Wang, Y. Zhao, C. Sun, H. Xu and J. Zhao, *J. Alloy Compd.*, **861**, 157995 (2021).
50. J. Yang, T. Xie, Q. Zhu, J. Wang, L. Xu and C. Liu, *J. Mater. Chem. C*, **8**, 2579 (2020).
51. Z. S. Seddigi, M. A. Gondal, U. Baig, S. A. Ahmed, M. A. Abdulaziz, E. Y. Danish, M. M. Khaled and A. Lais, *PloS One*, **12**, e0172218 (2017).
52. L. Zhang, T. Xu, X. Zhao and Y. Zhu, *Appl. Catal. B: Environ.*, **98**, 138 (2010).
53. P. Dumrongrojthanath, T. Thongtem, A. Phuruangrat and S. Thongtem, *Res. Chem. Intermed.*, **42**, 5087 (2016).
54. I. Matsuura, R. Schut and K. Hirakawa, *J. Catal.*, **63**, 152 (1980).
55. K. M. Koczkur, S. Mourdikoudis, L. Polavarapu and S. E. Skrabalak, *Dalton Trans.*, **44**, 17883 (2015).
56. X. Li, D. Wu, J. Yang, Q. Zhu, J. Wang, Y. Peng, T. Xie and H. Chen, *Sol. Energy*, **220**, 440 (2021).
57. M. Thommes, K. Kaneko, A. V. Neimark, J. P. Olivier, F. Rodriguez-Reinoso, J. Rouquerol and K. S. W. Sing, *Pure Appl. Chem.*, **87**, 1051 (2015).
58. P. Sun, F. Teng, Z. Yang, X. Yang, S. Zhai, S. Liang, W. Gu, W. Hao and S. Shi, *J. Mater. Chem. C*, **8**, 2475 (2020).
59. N. Tahmasebi, H. Esmaeilpour, F. Movahedifard, A. Hakimyfard and H. Moayeri, *Mater. Sci. Semicond. Process.*, **131**, 105876 (2021).
60. B. Li and Y. Wang, *J. Phys. Chem. Solids*, **72**, 1165 (2011).
61. M. A. Johar, R. A. Afzal, A. A. Alazba and U. Manzoor, *Adv. Mater. Sci. Eng.*, **2015**, 1 (2015).
62. K. Kaviyarasu, C. M. Magdalane, D. Jayakumar, Y. Samson, A. K. H. Bashir, M. Maaza, D. Letsholathebe, A. H. Mahmoud and J. Kennedy, *J. King Saud Univ. Sci.*, **32**, 1516 (2020).
63. C. M. Magdalane, K. Kaviyarasu, G. M. A. Priyadharsini, A. K. H. Bashir, N. Mayedwa, N. Matinise, A. B. Isaev, N. A. Al-Dhabi, M. V. Arasu, S. Arokiyaraj and J. Kennedy, *J. Mater. Res. Technol.*, **8**, 2898 (2019).
64. Y. Ao, K. Wang, P. Wang, C. Wang and J. Hou, *RSC Adv.*, **6**, 48599 (2016).
65. K. Wang, C. Shao, X. Li, X. Zhang, N. Lu, F. Miao and Y. Liu, *Catal. Commun.*, **67**, 6 (2015).
66. F. Mokhtari and N. Tahmasebi, *J. Phys. Chem. Solids*, **149**, 109804 (2021).
67. X. Chang, M. A. Gondal, A. A. Al-Saadi, M. A. Ali, H. Shen, Q. Zhou, J. Zhang, M. Du, Y. Liu and G. Ji, *J. Colloid Interface Sci.*, **377**, 291 (2012).

# Supporting Information

# PVP-assisted hydrothermal synthesis of $BiOCl/Bi_2Mo_3O_{12}$ photocatalyst for decolorization of rhodamine B under visible-light irradiation

**Azadeh Khane*, Nemat Tahmasebi**,†, and Hesam Seyed Kaboli*,†**

*Department of Civil Engineering, Jundi-Shapur University of Technology, Dezful, Iran
**Department of Physics, Jundi-Shapur University of Technology, Dezful, Iran
(*Received 2 August 2021 • Revised 6 December 2021 • Accepted 13 December 2021*)

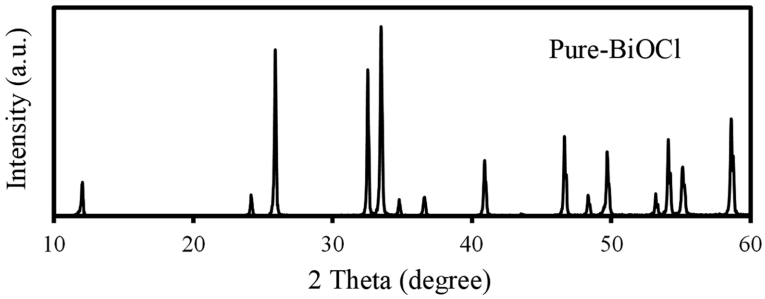


**Fig. S1. XRD patterns of pure-BiOCl sample.**

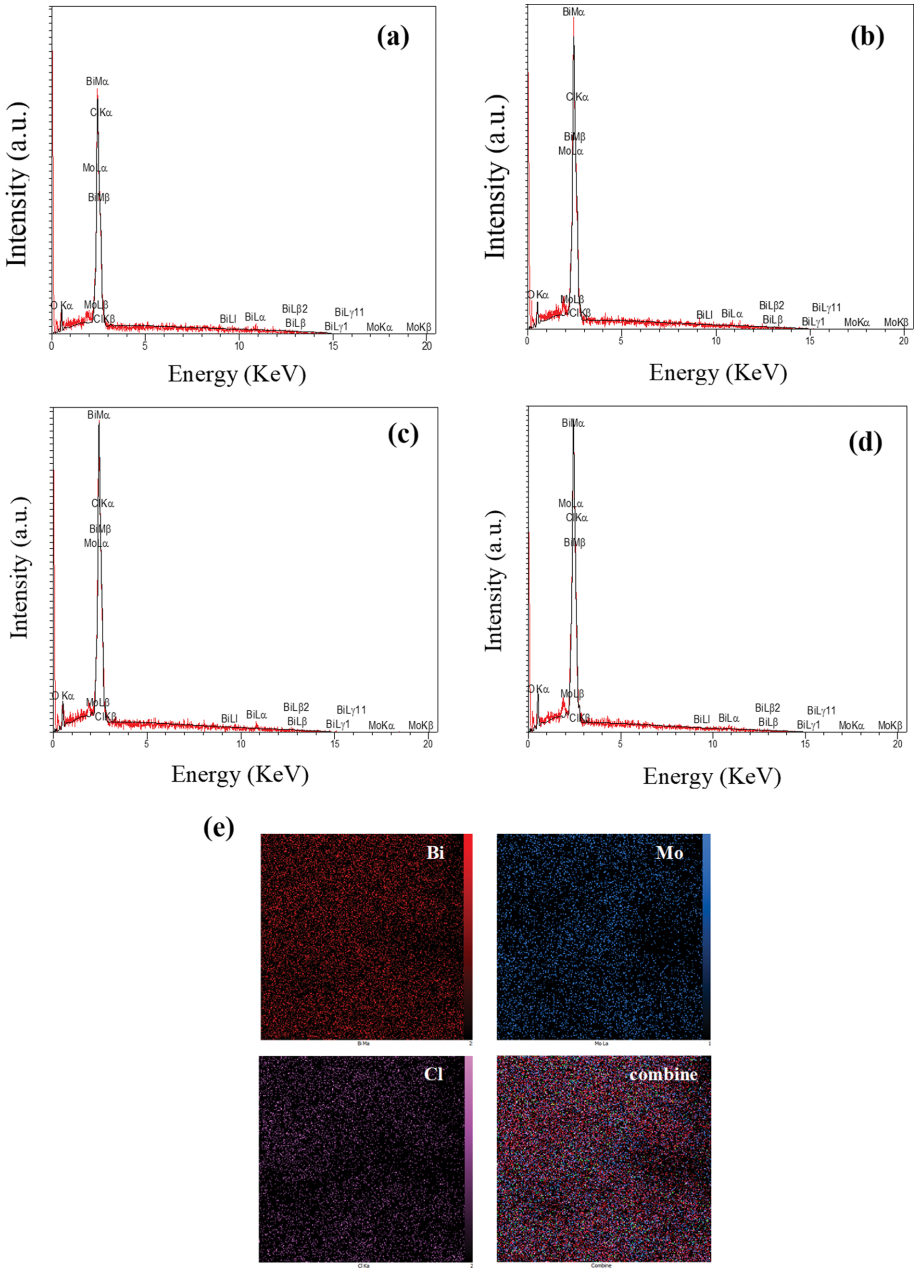


**Fig. S2. The EDS spectrum of samples (a) P-0, (b) P-0.1, (c) P-0.3 and (d) P-0.5, and (e) elemental mapping of P-0.1.**

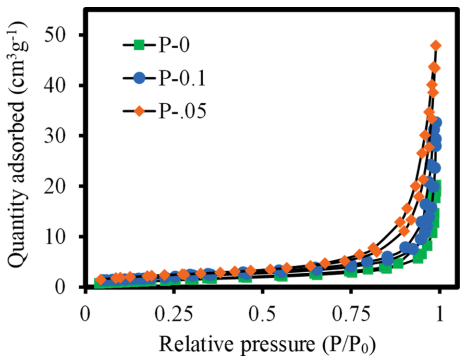


**Fig. S3. The nitrogen adsorption-desorption isotherm of P-0, P-0.1 and P-0.5.**

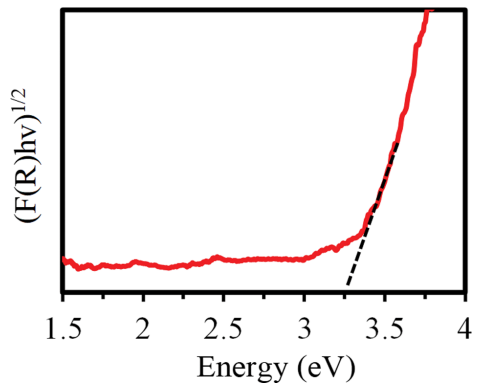


**Fig. S4. Band gap of pure-BiOCl.**